Progress In Electromagnetics Research B, Vol. 111, 111–124, 2025

PIER B

(Received 20 January 2025, Accepted 1 April 2025, Scheduled 16 April 2025)

Implications of Secondary Electron Yield of the Material States Related to Spacecraft Life Span on Absolute Charging of Pyramidal Horn Antenna

Ashish Pandya[1], Nikhil Kothari[1], Rizwan Alad[1,*], Suryakant Gupta[2], and Keyurkumar Patel[1]

[1]*Dharmsinh Desai University, Nadiad, Gujarat, India*
[2]*FCIPT — Institute for Plasma Research, Gandhinagar, Gujarat, India*

ABSTRACT: Accurately estimating spacecraft charging requires consideration of an appropriate secondary electron yield (SEY) of spacecraft materials. SEY is influenced by factors such as surface roughness, oxidation, and contamination. Using SEY values for materials not representative of actual spacecraft conditions can lead to significantly inaccurate spacecraft charging predictions. Against the use of default values for smooth and clean elemental aluminum (Al), this work examines the impact of SEY of Al in its relevant states over a spacecraft's lifespan in favour of the reliable estimation of absolute charging. It specifically focuses on the impact of SEY on the absolute charging of a pyramidal horn antenna, one of the essential spacecraft modules. For modeling of charging, the antennas are assumed to be in appropriate states of Al, i.e., oxidized Al for the beginning of life and Al with thin Carbon (C) — rich contamination for the end-of-life of a spacecraft. The observed deviation in absolute charging will determine a more realistic approach to protect a spacecraft against Electrostatic Discharge (ESD).

1. INTRODUCTION

Surface charging induced Electrostatic Discharge (ESD) is one of the most notorious events of space environment, leading to mission termination [1]. Spacecraft bodies orbiting around the geosynchronous orbit (GEO) plasma environment are charged with exceptionally higher negative potential during geomagnetic substorm events. Such higher absolute charging and the greater mobility of electrons cause the emission of ESD current. This ESD current releases the accumulated charge stored in the capacitance between the spacecraft structure and ambient plasma. The initial stage of absolute charging may progress towards its subsequent stages of differential charging and eventually, ESD because of dissimilar induced electron yields and different sunlit conditions on the adjacent surfaces of a spacecraft [2, 3]. On account of the ESD occurrences on subsystems of a satellite such as various antennas and solar arrays, several satellites in the past suffered from anomalous commands, circuit shorts, and eventually triggered premature weapon ignition on various payloads [1–3]. In view of possibility of catastrophic consequences, accurate computation of absolute charging has been considered critically essential to predict the ESD events and protect the satellites.

In view of this, several works related to this phenomenon have been reported recently in the literature [4–8]. In order to study and analyze the phenomenon of charging and ESD on a spacecraft structure, estimation of the capacitance of different geometrical shapes used in spacecraft bodies is imperative. Detailed assessment of capacitance for different geometrical shapes of a spacecraft such as rectangular plate, square plate, circular disk, rectangular cuboid, dielectric coated metallic parallelepiped cylinder, cuboid with plates, and pyramid has been presented in [9–15]. A spacecraft structure is also composed of dual bodies such as conical metallic structures in the form of funnels oriented skewed or coaxial to each other. The computation of capacitances of these structures is reported earlier in [16]. However, absolute capacitance of isolated pyramidal horn antenna structure is not available in the literature. Note that horn antenna is an essential module in a spacecraft as a feeder for large antenna structures of parabolic dish antennas, besides its use in calibration of other high gain antennas and measurement of electromagnetic interference measurements on board [17]. Moreover, a coupled horn antenna module is included in a satellite assembly [17]. Hence, the computation of its capacitance and charge distribution is of practical interest. This will in turn facilitate the estimation of the lumped circuit capacitance model of a spacecraft and, subsequently, its charging caused by harsh ambient plasma.

SEY (secondary electron yield) and BEY (backscattered electron yield) are the major contributors to the number of outgoing electrons from a material surface and enforce the spacecraft surface to float at a more positive potential. Computation has to include dominant currents of SEY and BEY for reliable estimation. In the recent past, absolute charging of a spacecraft modeled as a rectangular cuboid and two plates with parabolic reflector antennas have been computed [12, 13]. The analysis of this model presented in these works lacks dominant currents of SEY and BEY. Recently, these currents have been included in [14] in the analysis of the charging of a metallic pyramid of Aluminum (Al) using the formulation of Whipple [18]. Despite

---

* Corresponding author: Rizwan Habibbhai Alad (rizwan_alad.ec@ddu.ac.in).

the fact that better SEY formulations have been made available in the past [19], the characterization of SEY in absolute charging and the corresponding estimation is till an active area of research.

The earlier research is based on the NASCAP (NASA Charging Analyzer Program) default values for smooth and clean elemental Al [14, 20–26]. Aging related surface modification significantly affects SEY [27–29]. Hence, the consideration of clean Al is inappropriate. In view of this, SEY values of Al with rough surfaces and thicker oxide layers, and technical Al with thin C-rich contamination are recommended over SEY values of clean Al with smooth surfaces for beginning-of-life and end-of-life space simulations, respectively [27].

The research presented in this paper (i) computes the surface charge distribution and capacitance of an isolated pyramidal and coupled pyramidal horn antenna using Method of Moments (MoM), (ii) studies the impact of SEY formulations of Whipple [18] and Katz et al. [19] on the estimation of absolute charging, (iii) investigates the implication of SEY of the appropriate states of Al against clean Al on absolute charging estimation of these structures. To investigate the effect of the states of Al on absolute charging, we conducted analysis using a single Maxwellian plasma model. Our findings indicate deviations from the results in the previous studies that utilized clean elemental Al and highlight the necessity of considering material state variations in charging predictions. For realistic computations, the antennas are assumed to be of different extents of oxidized Al for the beginning of life and Al with thin Carbon (C) — rich contamination for end-of-life modeling of charging.

2. FORMULATION OF SURFACE CHARGING MODEL AT GEO

A spacecraft stumbles upon GEO plasma-induced and material-depended currents. The resulting transient variation of body potential on a spacecraft structure from this spacecraft plasma interaction is obtained by [2],

$$C_{body}\frac{dV}{dt} = j_{net}A \tag{1}$$

where j_{net} is a net current density due to space plasma, C_{body} the body capacitance model of a structure with respect to ambient neutral plasma, V the body potential, and A the surface area of a structure. Figure 1 shows the methodology to estimate absolute charging of a spacecraft across its lifespan. The GEO plasma distribution is characterized by single Maxwellian plasma model. The potential on a spacecraft surface due to interactions with the plasma is determined by solving the balance of currents leaving and striking the surface at equilibrium. The body capacitance (C_{body}) of the spacecraft geometrical surface, which governs the transient variation of the potential, is computed using the MoM. Subsequently, the resultant differential equation of surface charging is numerically integrated which provides a transient variation of body potential on a material surface. We find absolute charging for different values of SEY corresponding to the material state variations across a spacecraft lifespan.

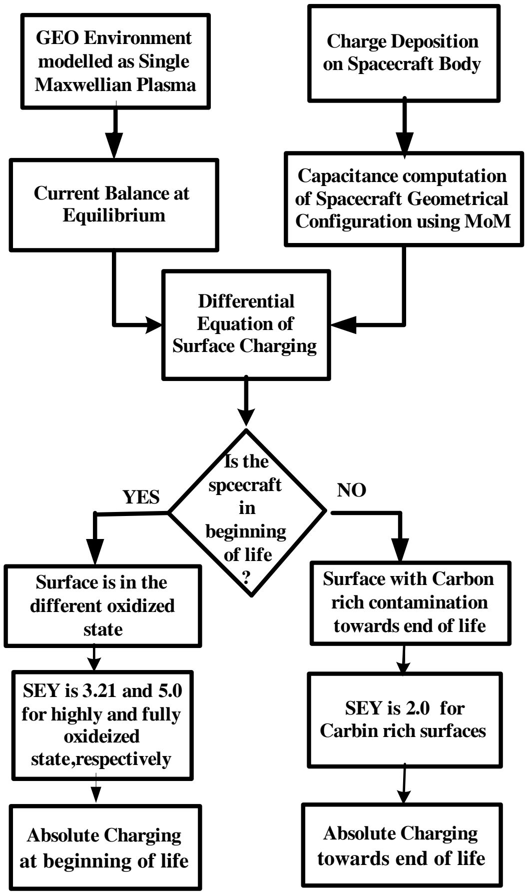

FIGURE 1. Absolute charging estimation of spacecraft across its lifespan.

A spacecraft collects zero net current from GEO plasma at equilibrium and is indicated by the fundamental current balance expression of the spacecraft charging [1],

$$J_{net} = \sum J_{in} + \sum J_{out} = 0 \tag{2}$$

where $\sum J_{in} = -j_e$, and $\sum j_{out} = j_i + j_{se} + j_{be} + j_{si}$.

Here, J_{net} is the total incident current density due to space plasma; j_e and j_i are environmental induced electron and ion current density; j_{se} and j_{be} are secondary emitted electron current density and backscattered electron current density due to electrons, respectively; and j_{si} is secondary electron current density due to ions.

Further analysis of Eq. (2) follows orbit motion limited (OML) regime relevant for the spacecraft charging in the GEO environment. Accordingly, the net current density for single Maxwellian plasma distribution for a sphere owing to repelled species with body potential, $V < 0$, is given by [3],

$$\begin{aligned} & j_{net} = -j_e + j_i + j_{se} + j_{be} + j_{si} \\ & \text{where } j_e = -j_{0e}\exp\left(\frac{eV}{kT_e}\right),\ j_i = j_{0i}\left(1 - \frac{eV}{kT_e}\right), \\ & \text{and } j_{0e,i} = \frac{1}{\sqrt{2\pi}} n_{e,i} e\left(\sqrt{\frac{kT_{e,i}}{m_{e,i}}}\right) \end{aligned} \tag{3}$$

Here j_{0e} and j_{0i} represent the electron and ion current density, respectively when spacecraft is not charged, i.e., charged with zero (0) potential. The Boltzmann constant is denoted by k. The density, temperature, and mass of electrons are denoted by n_e, T_e, and m_e, respectively. The density, temperature, and mass of ions are denoted by n_i, T_i, and m_i, respectively. The constant 'e' represents an absolute value of the electron charge, i.e., 1.6×10^{-19}C.

In order to solve Eq. (3) of the net current density, the following relationships of the expressions related to secondary and backscattered current density (j_{se}, j_{si}, and j_{be}) as well as particle energy are instrumental.

Secondary electron current density due to electrons is [30],

$$j_{se} = e\left(\frac{2\pi}{m_e^2}\right)\int_0^{\infty} Y_{se}\left(E\right) E f\left(E\right) dE \exp\left(\frac{eV}{kT_e}\right) \quad (4)$$

where Y_{se} and E are electron-induced SEY and incident electron energy, respectively. Single Maxwellian space plasma velocity distribution of species "s" (electrons and ions) is given by $f(E)$ [1],

$$f\left(E\right) = n_s\left(\frac{m_s}{2\pi kT_s}\right)^{3/2} \exp\left(\frac{-E}{kT_s}\right), \quad E = \frac{1}{2}m_s v_s^2 \quad (5)$$

where f is the distribution function expressed in sec^3/cm^6; n_s is the density of species "s" expressed in cm^{-3}; T_s is the temperature of species "s" expressed in eV; m_s is the mass of species "s" expressed in kg; v_s denotes the velocity of species "s" expressed in cm/sec.

The dependence of Y_{se} (SEY) in Eq. (4) on an angle of incidence (θ) and energy (E) of the incident electrons is given by [18],

$$Y_{se} = \frac{1.114\delta_m}{\cos\theta}\left(\frac{E_m}{E}\right)^{0.35}\left\{1 - \exp\left[-2.28\cos\theta\left(\frac{E}{E_m}\right)^{1.35}\right]\right\} \quad (6)$$

where E_m is the primary energy corresponding to the maximum yield (δ_m). We employ two widely used SEY formulations proposed by Whipple [18] and Katz et al. [19]. Because of the dependence of SEY on incidence angle (θ), the absolute charging must be analyzed for isotropic and normal incidences [18]. Its expressions are listed in Appendix A [18, 19].

Secondary electron current density (j_{si}) due to ions is given as [30],

$$j_{si} = e\left(\frac{2\pi}{m_i^2}\right)\int_0^{\infty} Y_{si}\left(E - eV\right) E f\left(E\right) dE \left(1 - \frac{\mathrm{eV}}{\mathrm{kT_i}}\right) \quad (7)$$

The expression for Ion-induced SEY (Y_{si}) for isotropic and normal incidences is listed in Appendix A [31].

Backscattered electron current density (j_{be}) due to electrons is represented as [30],

$$j_{be} = e\left(\frac{2\pi}{m_e^2}\right)\int_0^{\infty} Y_{be}\left(E\right) E f\left(E\right) dE \exp\left(\frac{eV}{kT_e}\right) \quad (8)$$

BEY (Y_{be}) for both the incidences is obtained from the incident electron energy (E) and the material atomic number (Z) with the expressions followed from [31]. Total incident surface current density (j_{net}) due to space plasma interaction as a function of the body potential (V) is computed using Eq. (2) through Eq. (8).

Next, we compute the requisite surface charge distribution and free space capacitance to find the ESD prone sites and the absolute charging of spacecraft structures. Free space capacitance, C_{body}, depends on spacecraft assembly with its modules. This paper addresses the problem of absolute charging of the essential structures of a spacecraft assembly, horn antennas. The capacitance estimation of two different cases of the structure, (i) isolated pyramidal horn antenna and (ii) coupled pyramidal horn antennas using MoM, is discussed below.

2.1. Capacitance of an Isolated Pyramidal Horn Antenna

Consider the pyramidal horn antenna of Fig. 2(a) in a Cartesian coordinates system. It consists of two parts: (i) waveguide with length L, width W, and height H consisting of four rectangular plates, and (ii) horn aperture having four tilted trapezoidal plates given by flaring angle α and β as shown in Fig. 2(b) and Fig. 2(c), respectively. Horn has an aperture with E-plane width of A and H-plane height of B.

From the geometry in Fig. 2, flare angles and various lengths are given by:

$$\begin{gathered}\tan\left(\alpha\right) = \frac{A}{2R_a} \quad \tan\left(\beta\right) = \frac{B}{2R_b} \\ R_a = \frac{A}{A - W}R_A, \quad R_b = \frac{B}{B - H}R_B, \\ L_a^2 = R_a^2 + \frac{A^2}{4}, \quad L_b^2 = R_b^2 + \frac{B^2}{4}\end{gathered} \quad (9)$$

R_A and R_B, the perpendicular distances from the plane of the waveguide opening to the plane of the horn, must be equal, i.e., $R_A = R_B$. For the given horn sides A, B, and length R_A, Eq. (9) allows the computation of all relevant geometrical parameters required for the construction of the horn antenna.

In order to find the capacitance of the structure of Fig. 2(a), the unknown charge distribution on the structure must be computed by assuming known equipotential (Φ) metallic surface. The potential (Φ) at any observation point $r(x, y, z)$ due to charge distribution (ρ) at source point $r'(x', y', z')$ on eight conducting surface is given by [32],

$$\Phi = \frac{1}{4\pi\varepsilon}\left[\sum_{i=1}^{8}\int_{S_i}\frac{\rho\left(r'_i\right)}{\left|r - r'_i\right|}dS_i\right] \quad (10)$$

The integration is evaluated over the conductor surfaces denoted by S_i. The resulting integral equations can find unknown charge distributions ($\rho_1, \rho_2, \ldots, \rho_8$) on the surfaces using the MoM [32]. In order to apply the MoM, the pyramidal horn structure is divided into a number of rectangular subsections (N), as shown in Fig. 3.

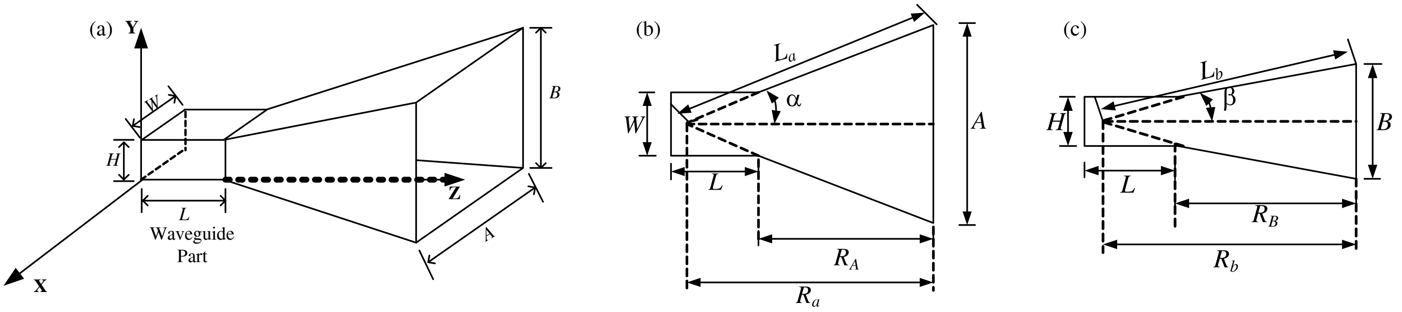

FIGURE 2. (a) Pyramidal horn antenna. (b) Top view. (c) Side view.

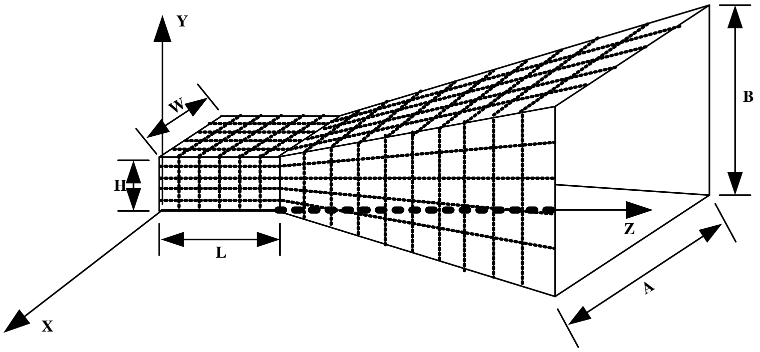

FIGURE 3. Pyramidal horn antenna with uniform rectangular sub-sections.

The unknown charge distribution (ρ) appearing in Eq. (10) is expressed using the point matching and delta function as the testing function [32].

$$\rho = \sum_{n=1}^{N} \alpha_n f_n \tag{11}$$

Here, α_n is an unknown coefficient representing charge per unit surface area of n^{th} subsection of a body, f_n the pulse basis function, and N the number of subsections.

The set of simultaneous equations obtained from Eq. (10) after substituting Eq. (11) and using point matching method with the help of Dirac delta function as the testing function is as follows:

$$\begin{aligned}\Phi_i = & \sum_{n=1}^{N_1} \alpha_{1n} l_{i1mn} + \sum_{n=N_1+1}^{N_1+N_2} \alpha_{2n} l_{i2mn} + \cdots \\ & + \sum_{n=N_1+N_2+\ldots+N_7+1}^{N_1+N_2+\ldots+N_8} \alpha_{8n} l_{i8mn}\end{aligned} \tag{12}$$

where $N_1, N_2, \ldots, N_8$ are subsections along the eight surfaces of the structure, respectively. Coefficients $l_{i1mn}, l_{i2mn}, \ldots, l_{i8mn}$ appearing in the above equations are represented in a generalized form as,

$$\begin{gathered} l_{mn} = \frac{1}{4\pi\varepsilon_0} \int\limits_{s_n} \frac{1}{|r_m - r'_n|} ds'_n \\ m = 1, \ldots, N \quad \text{and} \quad n = 1, \ldots, N \\ N = N_1 + N_2 + \ldots N_8 \end{gathered} \tag{13}$$

where ds'_n is an area of source subsection, and $r_m(x_m,\, y_m,\, z_m)$ is a matching point at the midpoint of each subsection in consideration.

The set of simultaneous equations of Eq. (12) for eight surfaces is transformed into an equation of matrices of the form,

$$\begin{bmatrix} \Phi_1 \\ \Phi_2 \\ \Phi_3 \\ \Phi_4 \\ \Phi_5 \\ \Phi_6 \\ \Phi_7 \\ \Phi_8 \end{bmatrix} = \begin{bmatrix} \alpha_{1n} \\ \alpha_{2n} \\ \alpha_{3n} \\ \alpha_{4n} \\ \alpha_{5n} \\ \alpha_{6n} \\ \alpha_{7n} \\ \alpha_{8n} \end{bmatrix} \begin{bmatrix} [l_{11}] & [l_{12}] & [l_{13}] & [l_{14}] & [l_{15}] & [l_{16}] & [l_{17}] & [l_{18}] \\ [l_{21}] & [l_{22}] & [l_{23}] & [l_{24}] & [l_{25}] & [l_{26}] & [l_{27}] & [l_{28}] \\ [l_{31}] & [l_{11}] & [l_{33}] & [l_{34}] & [l_{35}] & [l_{11}] & [l_{37}] & [l_{38}] \\ [l_{41}] & [l_{42}] & [l_{43}] & [l_{44}] & [l_{45}] & [l_{46}] & [l_{47}] & [l_{48}] \\ [l_{51}] & [l_{52}] & [l_{53}] & [l_{54}] & [l_{55}] & [l_{56}] & [l_{57}] & [l_{58}] \\ [l_{61}] & [l_{62}] & [l_{63}] & [l_{64}] & [l_{65}] & [l_{66}] & [l_{67}] & [l_{68}] \\ [l_{71}] & [l_{72}] & [l_{73}] & [l_{74}] & [l_{75}] & [l_{76}] & [l_{77}] & [l_{78}] \\ [l_{81}] & [l_{82}] & [l_{83}] & [l_{84}] & [l_{85}] & [l_{86}] & [l_{87}] & [l_{88}] \end{bmatrix} \tag{14}$$

This system of linear equations in Eq. (14) is solved by the generalized minimum residual (GMRES) iterative algorithm [33] to determine charge density on each conducting surface. The unknown charge density is represented as,

$$\begin{bmatrix} \alpha_{1n} \\ \alpha_{2n} \\ \alpha_{3n} \\ \alpha_{4n} \\ \alpha_{5n} \\ \alpha_{6n} \\ \alpha_{7n} \\ \alpha_{8n} \end{bmatrix} = \begin{bmatrix} [\zeta_{11}] & [\zeta_{12}] & [\zeta_{13}] & [\zeta_{14}] & [\zeta_{15}] & [\zeta_{16}] & [\zeta_{17}] & [\zeta_{18}] \\ [\zeta_{21}] & [\zeta_{22}] & [\zeta_{23}] & [\zeta_{24}] & [\zeta_{25}] & [\zeta_{26}] & [\zeta_{27}] & [\zeta_{28}] \\ [\zeta_{31}] & [\zeta_{11}] & [\zeta_{33}] & [\zeta_{34}] & [\zeta_{35}] & [\zeta_{36}] & [\zeta_{37}] & [\zeta_{38}] \\ [\zeta_{41}] & [\zeta_{42}] & [\zeta_{43}] & [\zeta_{44}] & [\zeta_{45}] & [\zeta_{46}] & [\zeta_{47}] & [\zeta_{48}] \\ [\zeta_{51}] & [\zeta_{52}] & [\zeta_{53}] & [\zeta_{54}] & [\zeta_{55}] & [\zeta_{56}] & [\zeta_{57}] & [\zeta_{58}] \\ [\zeta_{61}] & [\zeta_{62}] & [\zeta_{63}] & [\zeta_{64}] & [\zeta_{65}] & [\zeta_{66}] & [\zeta_{67}] & [\zeta_{68}] \\ [\zeta_{71}] & [\zeta_{72}] & [\zeta_{73}] & [\zeta_{74}] & [\zeta_{75}] & [\zeta_{76}] & [\zeta_{77}] & [\zeta_{78}] \\ [\zeta_{81}] & [\zeta_{82}] & [\zeta_{83}] & [\zeta_{84}] & [\zeta_{85}] & [\zeta_{86}] & [\zeta_{87}] & [\zeta_{88}] \end{bmatrix} \begin{bmatrix} \Phi_1 \\ \Phi_2 \\ \Phi_3 \\ \Phi_4 \\ \Phi_5 \\ \Phi_6 \\ \Phi_7 \\ \Phi_8 \end{bmatrix} \tag{15}$$

where $[\xi_{ijmn}]$ denotes elements of the inverse of $[l_{ijmn}]$ given in Eq. (14). Thus, the total charge on the structure is evaluated by,

$$Q=\sum_{n=1}^{N_1} \alpha_{1n}\Delta s_{1n}+\sum_{n=1}^{N_2} \alpha_{2n}\Delta s_{2n}+\ldots+\sum_{n=1}^{N_8} \alpha_{8n}\Delta s_{8n} \tag{16}$$

Free space capacitance ($C_{isolated}$) of the isolated horn antenna with respect to ambient neutral plasma is calculated by,

$$C_{isolated} = \frac{Q}{\Phi} \tag{17}$$

2.2. Capacitance of an Coupled Pyramidal Horn Antenna

Figure 4 shows two coupled pyramidal horn antennas separated by a finite coupling distance D along Y-axis with identical dimensions. From here, $A_1 = A_2$, $B_1 = B_2$, $R_{A1} = R_{A2} = R_{B1} = R_{B2}$, $R_a = R_b$, $L_1 = L_2$, $W_1 = W_2$, and $H_1 = H_2$,

To find the capacitance of the above structure, we assume that the two conductors are maintained at uniform potentials of Φ_1 and Φ_2, respectively. Using the concept of superposition [16], we can represent the relationship between the charges and potential in the matrix form of linear equations:

$$\begin{bmatrix} Q_1 \\ Q_2 \end{bmatrix} = \begin{bmatrix} C_{11} & C_{12} \\ C_{21} & C_{22} \end{bmatrix} \begin{bmatrix} \Phi_1 \\ \Phi_2 \end{bmatrix} \tag{18}$$

where Q_1 and Q_2 are the charges on two pyramidal horn antennas. C_{ii} and C_{ij} represent the self and coupled capacitances of the two antennas, respectively.

In order to apply the MoM, all conductor surfaces are divided into a large number of rectangular sub-sections, as shown in Fig. 4.

Following the method applied previously in Subsection 2.1, the unknown charge densities (α_{1n} and α_{2n}) are obtained as,

$$\begin{bmatrix} [\alpha_{1n}] \\ [\alpha_{2n}] \end{bmatrix} = \begin{bmatrix} \xi_{11mn} & \xi_{12mn} \\ \xi_{21mn} & \xi_{22mn} \end{bmatrix} \begin{bmatrix} \Phi_1 \\ \Phi_2 \end{bmatrix} \tag{19}$$

where ξij_{mn}; i, $j = 1.2$ denotes elements of the inverse of lij_{mn}; i, $j = 1.2$.

Comparison of Eq. (18) and Eq. (19) shows that the sum of the elements of each sub-matrix can be evaluated as an element of the capacitance matrix appearing in Eq. (18). The expressions for capacitance matrices are given by,

$$\begin{aligned} C_{11} &= \sum_{m=1}^{P_1} \sum_{n=1}^{P_2} \xi_{11mn} \times S_1 \\ C_{12} &= \sum_{m=P_1+1}^{P_1+P_2} \sum_{n=1}^{P_1} \xi_{12mn} \times S_1 \\ C_{21} &= \sum_{m=1}^{P_1} \sum_{n=P_1+1}^{P_1+P_2} \xi_{21mn} \times S_2 \\ C_{22} &= \sum_{m=P_1+1}^{P_1+P_2} \sum_{n=P_1+1}^{P_1+P_2} \xi_{22mn} \times S_2 \end{aligned} \tag{20}$$

where C_{ij} is the charge on the conductor i, resulting from a unit potential applied to conductor j, under the condition that all other conductors are grounded. Here, i and j assume values ranging from 1 to 2. S_1 and S_2 refer to the surface areas of each horn antenna. P_1 and P_2 are the numbers of subsections along the surfaces of each horn antenna.

The coupled capacitance ($C_{coupled}$) per unit length (H) of the coupled structure is now determined by the following relationship [16],

$$C_{coupled} = \frac{C_{11}C_{22} - C_{12}^2}{C_{11} + C_{22} + 2C_{12}} \times \frac{1}{H} \tag{21}$$

Charge distribution and capacitance for the horn antenna structures of Fig. 2 and Fig. 4 have been numerically computed using Eq. (9) through Eq. (21). The results of charge distribution on spacecraft structures facilitate the prediction of the most likelihood sites of ESD and are discussed in the following section. Additionally, the numerical results of the steady-state body potential in the Maxwellian plasma environments with the help of these capacitances are also presented.

3. NUMERICAL RESULTS AND DISCUSSION

The primary objective of this work is to evaluate the implication of SEY of the appropriate states of Al against clean Al on absolute charging estimation of spacecraft structures. The results

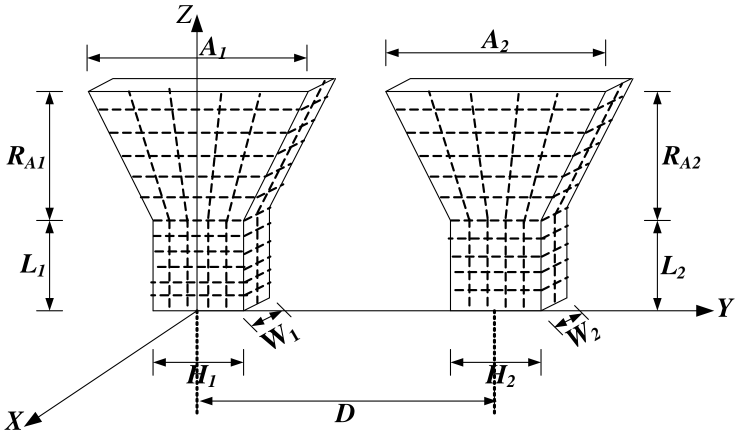

FIGURE 4. Two identical pyramidal horn antennas with uniform rectangular sub-sections.

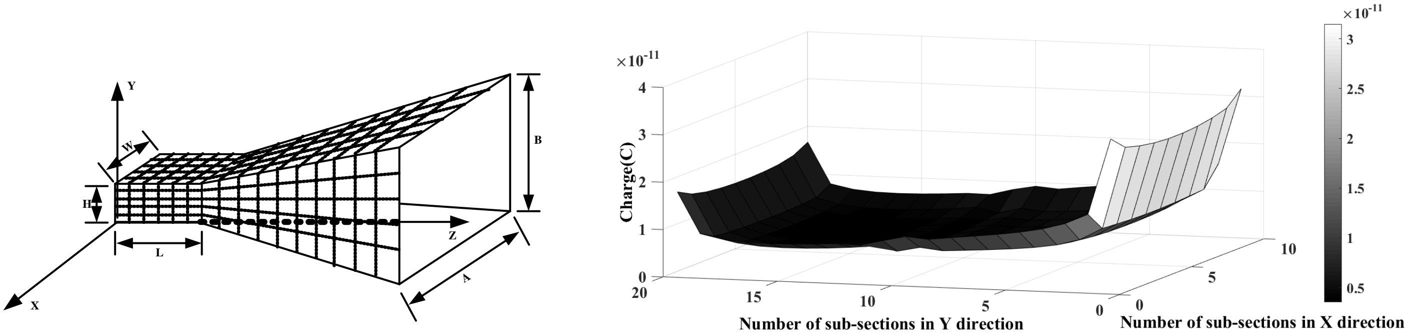

FIGURE 5. Axial charge distribution on pyramidal horn antenna.

obtained from the numerical analysis presented in the previous section are discussed in the following sections:

Based on the results of charge distribution and capacitance, we first validated the steady state body potential from the comparison of temporal profile of body potential of horn antenna structures with that of the spacecraft and its modules reported earlier [12–14, 20]. We employ SEY formulations proposed by Whipple [18] and Katz et al. [19] to examine the impact on absolute charging for clean Al structures. Subsequently, we study the effect of SEY of different Al states on charging and demonstrate the deviation from the results published earlier [14] with clean Al. Later, the charging is evaluated in the worst case of single Maxwellian plasma.

3.1. Charge Distribution and Capacitance

Numerical computations of charge distribution and free space capacitances have been carried out for the horn antenna structures using Eq. (9) through Eq. (21). The typical dimensions of the horn antenna structures of Fig. 2 and Fig. 4 are considered to be of $L \times W \times H = 1\,\text{m} \times 1\,\text{m} \times 0.5\,\text{m}$ and $A \times B \times C = 3\,\text{m} \times 1.5\,\text{m} \times 3\,\text{m}$. All charges on conductors are evaluated by considering uniform potential of 1 V. Both combined flat plate and tilted plate are subdivided into planar 10×10 subsections.

The sudden charge released during ESD from spacecraft structure is profoundly dependent on its geometry and the surface charge distribution. Fig. 5 depicts axial charge distribution in the XY plane of the horn antenna. The charge distribution on the flat and tilted metallic plate shoots up at the edges and is relatively flat at the middle portion of the plate, as observed in Fig. 5. The accumulation of higher charges at the edges with a small radius of curvature builds a stronger electric field with a higher possibility of ESD at such locations. The examination of axial charge distribution on the individual tilted plate in Fig. 6 reveals dissimilarity in the peaks of the charge distributions on each end of the tilted plate. This is because one end of the tilted plate is isolated in free space while the opposite end is attached to the surface of a flat plate. Because of the higher peak at the isolated end, the possibility of ESD is higher at this end than the other, where the tilted plate is attached to a flat plate. Similar finding can be applied to the flat plate, where one end is isolated in free space while the opposite end is attached to the surface of a tilted plate.

By collectively adding the charges of each subsection for total numbers of 1170 and 2340 subsections, and applying Eq. (17) and Eq. (21), the converged values of the capacitances are 154.23 pF and 87.19 pF (for $D = 5\,\text{m}$) in the case of isolated pyramidal horn antenna and coupled pyramidal horn antenna, respectively. Impact of the coupling between the two pyramidal horn antennas on the capacitance is mentioned in Table 1 for different distances (D) between the two antennas along the Y-axis. The result of reduction in the total capacitance of the coupled structure with increasing distance between the identical structures is consistent with the results reported earlier for two identical cones [16]. Such reduction in the total capaci-

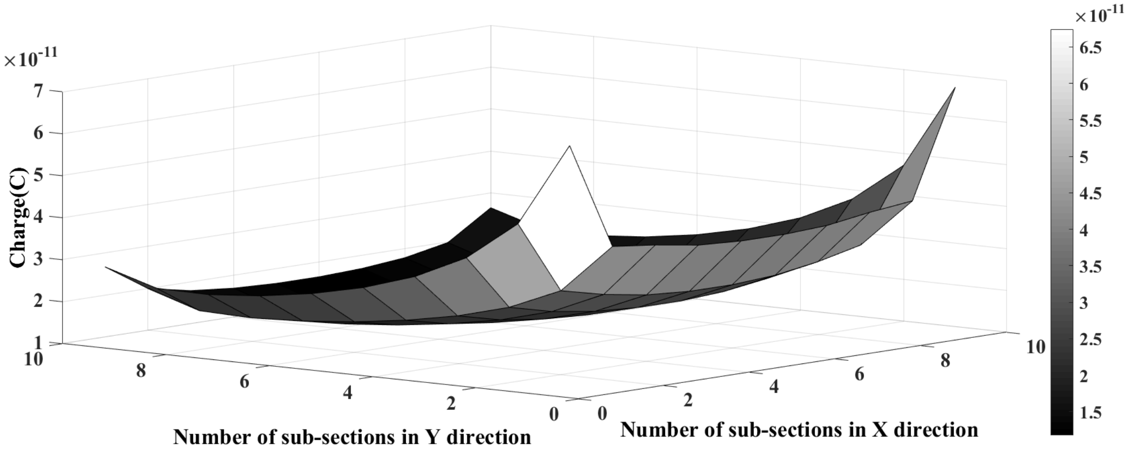

FIGURE 6. Axial charge distribution on tilted trapezoidal plate.

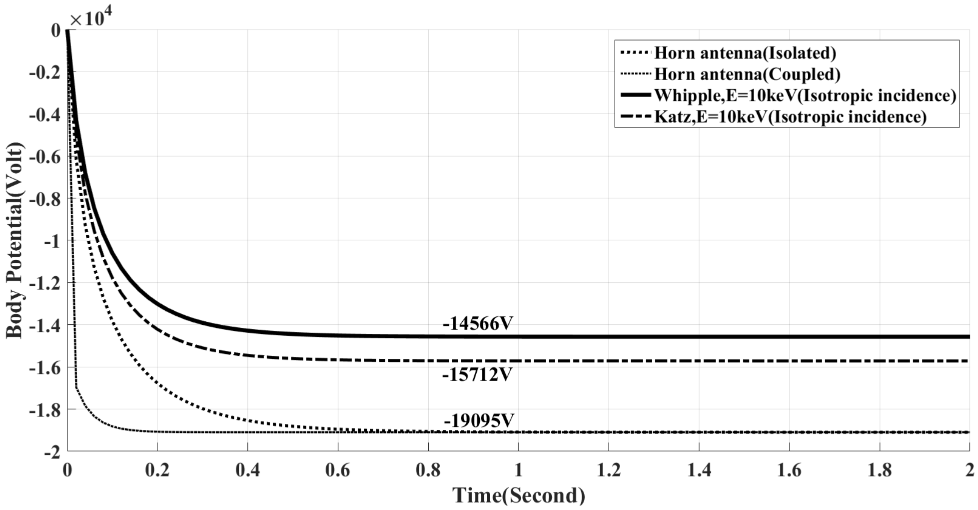

FIGURE 7. Body potential temporal variation ($\eta_e = \eta_i = 1.25 \times 10^6\,\mathrm{m}^{-3}$, $kT_e = 7.5\,\mathrm{keV}$, $kT_i = 10\,\mathrm{keV}$).

TABLE 1. Effect of change in distance on the capacitance of the coupled horn antennas.

Sr. No.	Distance D (m)	Capacitance (pF)
1	0.1	112.24
2	0.5	101.22
3	1	96.10
4	2	90.12
5	5	87.19

tance indicates that the distance is also an influencing factor on the temporal profile of the body potential of a spacecraft (To be discussed in the following section), which in turn, affects the total number of ESD events that a spacecraft must withstand.

3.2. Validation of Body Potential

The potential at steady-state signifies stability between surface potential and ambient potential of spacecraft structures which are based on the material properties and plasma environment. Therefore, despite differences in the area and capacitance of the structures, the results of earlier works [12–14, 20] can be applied to validate our numerical results of body potential. The validation of body potential computed as per our approach is initiated with the single Maxwellian plasma parameters ($\eta_e = \eta_i = 1.25 \times 10^6\,\mathrm{m}^{-3}$, $kT_e = 7.5\,\mathrm{keV}$, $kT_i = 10\,\mathrm{keV}$) of the earlier works [12–14, 20]. Note that in these works, the body potential is obtained without considering currents due to SEY-BEY and is designated as V_{ZEY} (ZEY-Zero Electron Yield) in this paper (Eq. (22)).

$$V_{ZEY} = \int \frac{1}{C_{body}}(-j_e + j_i)A dt \tag{22}$$

Here, j_e and j_i are evaluated from Eq. (3), and A is the surface area of the horn antenna structure. Fig. 7 illustrates body potential temporal variations for horn the antenna structures determined from Eq. (22). The results of the geometrical and electrical parameters presented in Table 2 provide comparison of the earlier works [12–14, 20] with our work in this paper. Identical values of the steady-state body potential of the structures investigated in this paper and the structures analyzed earlier [12–

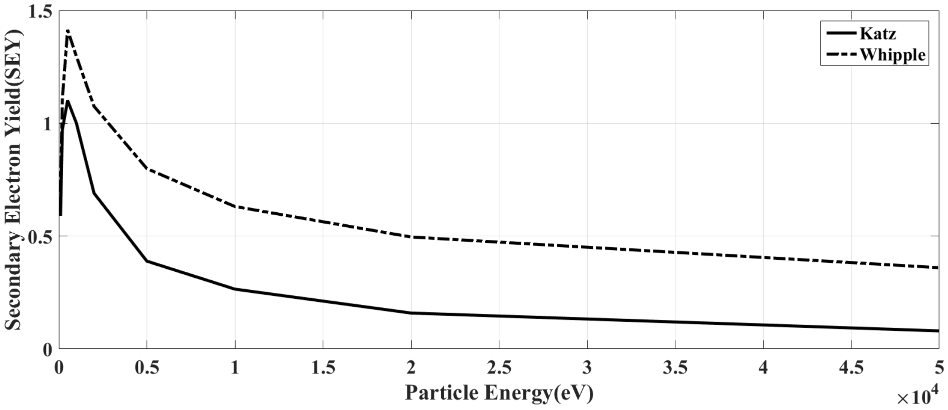

FIGURE 8. Comparison of SEY for different formulations.

TABLE 2. Comparison with the results of earlier works.

Geometry Parameters	Cuboid with Plates [12]	Cuboid with Plates [13]	Pyramid with Cuboid [14]	Spherical Object (OML) [20]	Isolated Horn Antenna	Coupled Horn Antenna ($D = 0.1$–5 m)
Area (m^2)	72	14.86	8.68	50.26	27	54
Capacitance (pF)	328.86	155.68	81.77	222.52	154.23	112.28–87.19
Body Potential (V)	-19095	-18779	-19095	-19094	-19095	-19095
Time (s)	1.258	2.560	1.10	1.2	1.37	0.43–0.36

14, 20] validate our computation. The temporal profile computed for each structure allows us to predict the time required to arrive at the ESD inception threshold, and subsequently ESD events are likely to occur over its lifetime. Due to differences in capacitance and area of the structures, the body potential temporal profiles demonstrate unequal slopes. Consequently, the coupled antenna attains the steady-state potential of -19095 V earlier (in 0.36 s–0.43 s corresponding to the distance of 5 m–0.1 m between two antennas) than the case of the isolated horn antenna (in 1.37 s), as observed in Table 2.

3.3. Estimation of Absolute Charging with SEY Formulations

In order to estimate the charging of satellite structures in the presence of SEY, several earlier works [14, 20, 22, 30, 36] based on numerical computation have applied Whipple model [18] and Katz formulation [19]. As the accuracy of SEY is a determining factor for a reliable charging analysis, it is worthwhile to study the impact of these SEY formulations on the estimation of absolute charging. Hence, the body potential ($V_{SEY-BEY}$) (Eq. (23)) for SEY-BEY related currents (Eqs. (24) and (25)) is computed initially for particle strike with the energy of 10 keV for an isolated horn antenna. As the particle energy up to a few tens of keV (50 keV) is responsible for surface charging [2], the investigation initially undertakes particle energy within this range. The charging analysis with respect to the entire particle energy range is discussed in Subsection 3.5.

$$V_{SEY-BEY}=\int\frac{1}{C_{body}}(-j_e+j_i+j_{se}+j_{be}+j_{si})Adt \tag{23}$$

$$j_{se,be}=e\left(\frac{2\pi}{m_e^2}\right)\int_0^{10keV} Y_{se,be}\left(E\right)Ef\left(E\right)dE\exp\left(\frac{eV}{kT_e}\right) \tag{24}$$

$$j_{si}=e\left(\frac{2\pi}{m_i^2}\right)\int_0^{10keV} Y_{si}\left(E-eV\right)Ef\left(E\right)\mathrm{dE}\left(1-\frac{\mathrm{eV}}{\mathrm{kT_i}}\right) \tag{25}$$

Here, j_e and j_i are evaluated from Eq. (3). The result of absolute charging for the isotropic incidence of particle strike is shown in Fig. 7. Because of the lesser SEY prediction of Katz model than the Whipple model as shown in Fig. 8, the amount of absolute charging (-15712 V) with Katz's formulation is 1146 V higher than that of Whipple's formulation (-14566). We find that the rise in absolute charging with the Katz's formulation decreases to 484 V for normal incidence. This is due to less prominent effect of normal particle incidence.

It is evident from its application in NASCAP-2k and SPIS that the Katz formulation is widely acceptable for SEY characterization. The Katz's formulation provides improved estimation of SEY through strong relations with characterized material parameters and possible future progress by considering the latest laboratory measurement results [19], which reflect in its higher absolute charging. Hence, the subsequent analysis of absolute charging in this paper adopts the Katz's formulation.

Although numerous previous studies on spacecraft charging have considered clean aluminum (Al) spacecraft structures [14, 15, 20–26], in reality, the surface state of Al changes due to prolonged exposure to the space environment [27–29]. This makes the assumption of clean Al structure in the charging analysis inappropriate because of the aging related surface

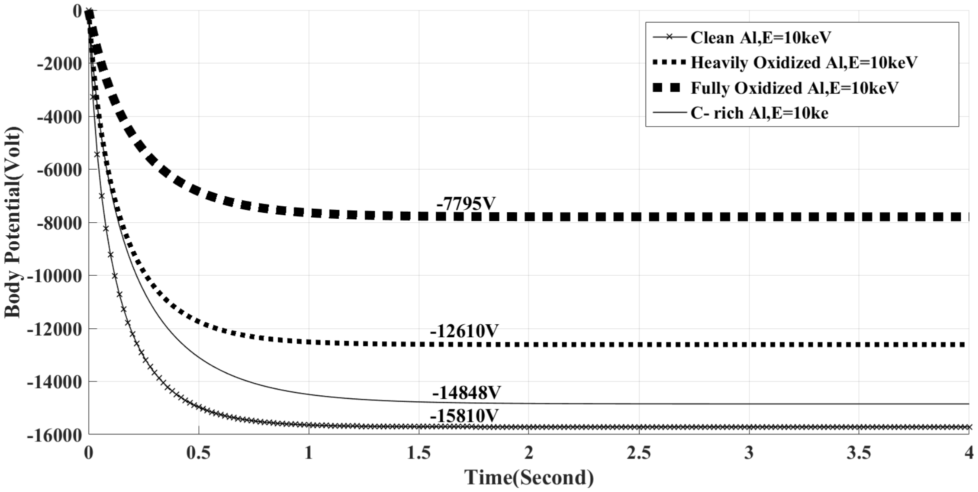

FIGURE 9. Body potential ($V_{SEY-BEY}$) temporal variation for isotropic incidence ($\eta_e = \eta_i = 1.25 \times 10^6\,\mathrm{m}^{-3}$, $kT_e = 7.5\,\mathrm{keV}$, $kT_i = 10\,\mathrm{keV}$) [12–14].

TABLE 3. Material parameters for the analysis [1, 18, 27–29].

Material	Electron-induced SEY		Ion-induced SEY		Atomic number
	δ_m	E_m (keV)	δ_1	E_m (keV)	Z
Clean Al	0.97	0.3	0.244	230	13
Heavily Oxidized Al	3.21	0.35			
Fully Oxidized Al	5.0	0.6			
C-rich Al	2.0	0.35			

modification. In view of this, SEY values of Al with rough surfaces and thicker oxide layers and technical Al with thin C-rich contamination are recommended over SEY values of clean Al with smooth surfaces for beginning-of-life and end-of-life space simulations, respectively [27]. Therefore, we carry forward the analysis for different extents of oxidized Al and C-rich Al in subsequent sections.

3.4. Implication in Charging Estimation for Different States of Al over Spacecraft Lifespan

SEY coefficients of various states of Aluminum with atomic number (Z) used in the computation of current densities due to SEY-BEY are listed in Table 3. Here, δ_m and δ_1 are peak emission coefficient for incident electrons and the incident ions with energy of 1 keV, respectively. The other parameter E_m is electron or ion energy corresponding to peak electron yield. The range of possible values of SEY (δ_m) for oxidized Al reported in literature is from 2.34 to 5.0, whereas for C-rich Al, it is from 1 to 2.5 [27–29]. Accordingly, we have carry out the analysis for some typical values from this range for oxidized Al, i.e., δ_m is 3.21 for heavy oxidized state, and δ_m is 5 for fully oxidized state. For C-rich Al, the analysis is performed for δ_m of 2.

Figures 9 and 10 illustrate the corresponding results of charging ($V_{SEY-BEY}$ as per Eq. (23)) for different states of Al under the isotropic and normal incidences of particles at 10 keV, respectively. Due to the significant increase in SEY (δ_m) of different states of oxidized Al and C-rich Al compared to clean Al as observed in Table 3, the body potential is significantly more positive than the earlier work [14] based on clean Al. The differences of more than 3000 V and 8000 V are observed between the charging results of clean Al (-15810 V) and heavily oxidized Al (-12610 V), and between clean Al (-15810 V) and fully oxidized Al (-7795 V), respectively for the isotropic incidence. For normal incidence, the differences are found to be ~ 700 V and ~ 1800 V. Such large deviations in results clearly reveal the consequence of the inappropriate consideration of clean Al structure in charging analysis.

Besides, it can be observed from Fig. 9 and Fig. 10 that the difference in charging across different extents of oxidization, i.e., between heavily oxidized Al and fully oxidized Al, is ~ 4800 V and ~ 1150 V, for isotropic and normal incidence, respectively. Moreover, there is an apparent difference in charging in the different states of oxidized Al (appropriate states for the beginning of life) and C-rich Al (appropriate state for the end-of-life) for both types of incidences. Such an immense difference in charging is due to the large variation in the electron yields between different states of oxidized Al and C-rich Al. Hence, the SEY variation in Al causes a significant variation in the charging level from the beginning of life (oxidized Al) to the end of life (C-rich) journey of a typical spacecraft surface. As reliable analysis of ESD needs correct estimation of absolute charging, the results presented in this work clearly indicate the necessity of considering the appropriate states of Al in the charging analysis.

The foregoing analysis of this paper adopted the plasma parameters from earlier works [12–14, 20] primarily to validate

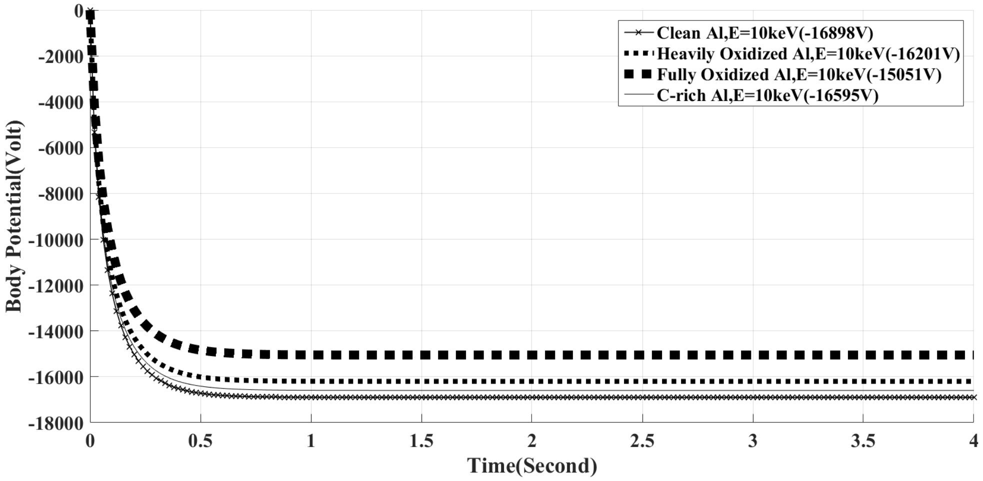

FIGURE 10. Body potential ($V_{SEY-BEY}$) temporal variation (Normal incidence) ($\eta_e = \eta_i = 1.25 \times 10^6\,\mathrm{m}^{-3}$, $kT_e = 7.5\,\mathrm{keV}$, $kT_i = 10\,\mathrm{keV}$) [12–14]. Here, $V_{SEY-BEY}$ refers to the body potential computed from Eq. (23) for SEY-BEY currents when the particle energy is 10 keV.

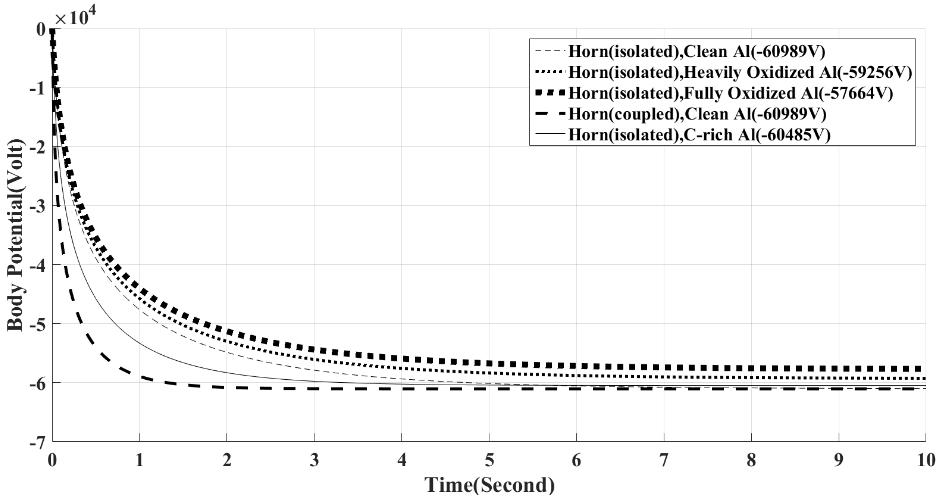

FIGURE 11. Body potential ($V_{SEY-BEY}$) transient profile in single Maxwellian worst case of plasma ($\eta_e = 1.2 \times 10^6\,\mathrm{m}^{-3}$, $\eta_i = 236 \times 10^3\,\mathrm{m}^{-3}$, $kT_e = 16\,\mathrm{keV}$, $kT_i = 29.5\,\mathrm{keV}$) [35]. Here, $V_{SEY-BEY}$ refers to the body potential computed from Eq. (23) for SEY-BEY currents when the particle energy is 10 keV.

the results obtained with our approach and demonstrate the deviation in the charging results while considering the spacecraft surface of clean Al. We continued the analysis further for the recommended cases related to the extreme temperature conditions known as the normal and worst cases of Maxwellian plasma environment. The normal case is a quiet plasma condition, whereas the worst case is characterized by significantly higher electron temperature than the normal case.

TABLE 4. Single Maxwellian recommended cases of plasma parameters [34, 35].

Parameters	Normal case	Worst case
η_e (m^{-3})	1.09×10^6	1.2×10^6
kT_e (keV)	4.83	16
η_i (m^{-3})	580×10^3	236×10^3
kT_i (keV)	14.5	29.5

3.5. Absolute Charging in Single Maxwellian Plasma Environment

The single Maxwellian plasma environment is simulated with parameters of Table 4. The normal case stands for an average body potential during a quite plasma state, whereas the worst case represents the largest negative body potential [14]. Because of the largest negative body potential in the worst case environment, the body potential temporal profile in such environment is one of the key factors in spacecraft design, and testing for the determination of the ESD events is likely to occur during a spacecraft lifetime [35]. Therefore, charging analysis adheres to this case of plasma environment from here onwards.

During the worst case with the particle energy of 10 keV for SEY-BEY currents, the body potential transient variations for the horn antenna structures are shown in Fig. 11. Apparently,

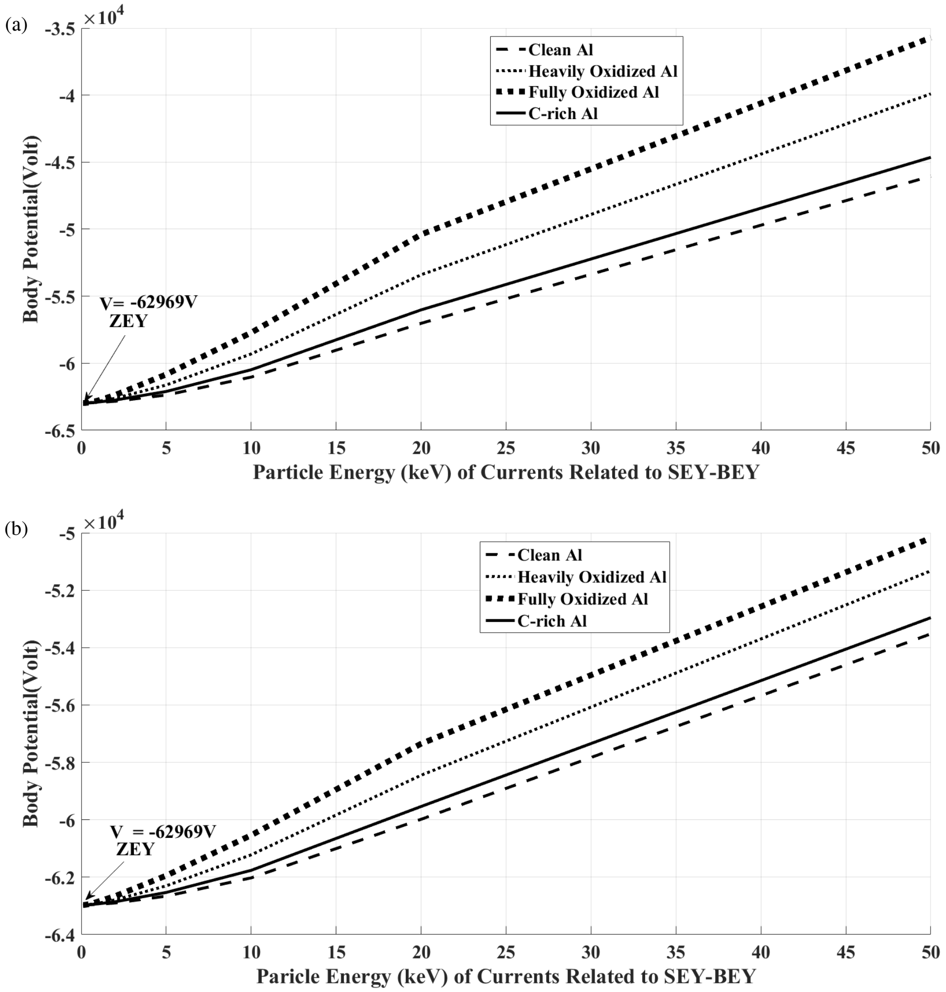

FIGURE 12. Body potential ($V_{SEY-BEY}$) versus particle energy of currents related to SEY-BEY ($\eta_e = 1.2 \times 10^6\,\mathrm{m}^{-3}$, $\eta_i = 236 \times 10^3\,\mathrm{m}^{-3}$, $kT_e = 16\,\mathrm{keV}$, $kT_i = 29.5\,\mathrm{keV})^{36}$ V_{ZEY} is the body potential obtained from Eq. (22) without considering currents due to SEY-BEY. (a) Isotropic Incidence. (b) Normal Incidence.

higher charging level of isolated horn antenna draws a longer time ($\sim$ 9 s) to attain the steady-state than the time ($\sim$ 1.37 s) noted from Fig. 7 with the previous set of plasma parameters used for validation. The observation is similar for the coupled horn antenna. While a greater time of attaining the steady-state can decrease ESD events over a spacecraft lifetime, the strength of ESD can be significantly higher due to greater charging.

Moreover, it is observed that the differences in the charging levels between clean Al (-60989 V) and heavy oxidized Al (-59256 V) and between clean Al (-60989 V) and fully oxidized Al (-57664 V) are as high as $\sim$ 1700 V and $\sim$ 3300 V, respectively. The deviations in the charging results shown above clearly indicate the impact of SEY in the respective material states, and accordingly the requirement of accommodating the variation occurring during a spacecraft life span.

To reinforce our findings, we extend the computations for a range of particle energy (up to 50 keV) responsible for surface charging [2]. The differences in the results of charging due to SEY modification among three states of Al for varying particle energy of SEY-BEY currents are shown in Fig. 12. The results of all material state demonstrate a greater positive charging than V_{ZEY} (V_{ZEY} is the body potential obtained without considering currents due to SEY-BEY as per Eq. (22)) with increasing particle energy of currents related to SEY-BEY. This trend is observed due to the increment in the total electron yield (which includes the electron and ion induced SEY, and electron induced BEY) with particle energy as shown in Fig. 13 [36]. The plot of electron and ion induced yields against particle energy in Fig. 13 is obtained for clean Al from the expressions reported in [18] and [19]. A similar trend is observed for the other states of Al. Note that SEY and BEY are the major contributors to the number of outgoing electrons from a material surface and enforce the spacecraft surface to float at a more positive potential.

Besides, the plots demonstrate significant difference in the charging with clean Al and different states of oxidized Al, whereas the difference in the different states of oxidized Al (appropriate states for the beginning of life) and C-rich Al (appropriate state for the end-of-life) is also clearly visible for both types of incidences.

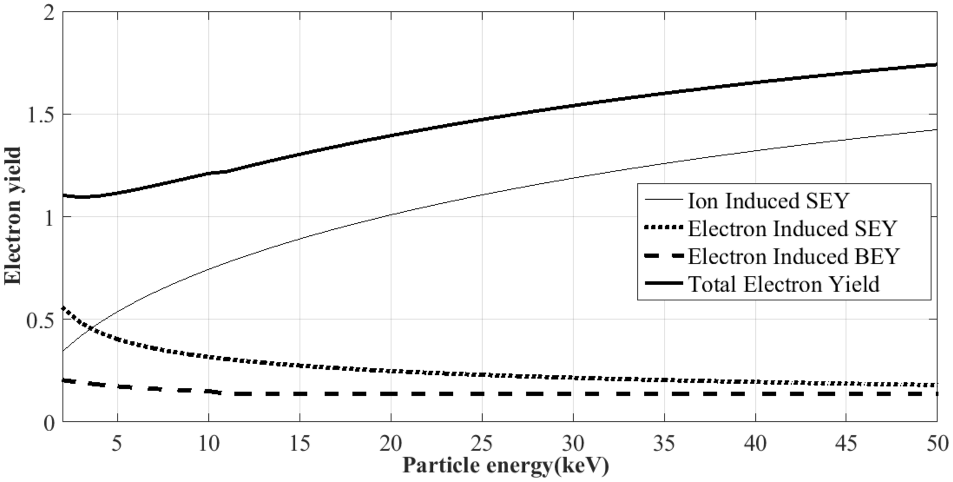

FIGURE 13. Electron yield vs. Particle energy [36].

4. CONCLUSION

Detailed investigations presented in this paper examine implications of SEY as well as the states of Al on surface charging in different conditions and environments related to space plasma. Our extensive analysis computes absolute charging of pyramidal horn antenna structures with SEY consideration of the most appropriate material states related to satellite life span. Major findings based on the electrostatic analysis carried out for the recommended single Maxwellian space plasma environments are summarized below.

(i) The edges of the structures are more prone to ESD than the middle portions due to higher charge accumulation. Additionally, the greater charge peak at isolated end of each plate reveals a higher possibility of ESD than the other end attached to the adjacent plate.

(ii) The distance between the coupled horn antennas influences the temporal profile of the spacecraft's body potential. Its variations inversely affect the total capacitance and saturation time, which in turn impacts the total number of ESD events. The computed values of capacitance are essential for the lumped circuit capacitance model for the charging analysis of an entire spacecraft.

(iii) There is a significant modification in the charging levels between clean Al and different states of oxidized Al. Such large deviations in results clearly reveal the consequence of the inappropriate consideration of clean Al structure in charging analysis. This finding is crucial for reliable estimation of the ESD events likely to occur during a spacecraft lifetime.

(iv) SEY variation in Al causes a significant variation in the charging level from the beginning of life (oxidized Al) to the end of life (C-rich) journey of a typical spacecraft surface for both particle incidences.

(v) The results of charging of different states of Al demonstrate a greater positive charging with increasing particle energy of currents related to SEY-BEY. Moreover, depending on the incident energy of the plasma, remarkable difference is observed in the charging results of different states of Al.

The consideration of clean Al spacecraft structures results in an unreliable estimation of absolute charging and, subsequently the strength of ESD due to its lesser SEY than oxidized state. The numerical results presented in this paper establish that the assumption of clean Al structure in the charging analysis is inappropriate as it does not accommodate the changes occurring because of the surface modifications.

APPENDIX A. FORMULATIONS OF SEY-BEY

A.1. Electron Induced SEY Formulation (Whipple) [18]

The dependence of Y_{se} (SEY) on an angle of incidence (θ) and energy (E) of the incident electrons is given by,

$$Y_{se}=\frac{1.114\delta_m}{\cos\theta}\left(\frac{E_m}{E}\right)^{0.35}\left\{1-\exp\left[-2.28\cos\theta\left(\frac{E}{E_m}\right)^{1.35}\right]\right\} \quad \text{(A1)}$$

For isotropic incidence (angle averaged particle strike on a spacecraft), Eq. (A1) is integrated to give an angle averaged SEY,

$$Y_{se}=\frac{2.228\delta_m}{Q}\left(\frac{E_m}{E}\right)^{0.35}\left(Q-1+e^{-Q}\right) \quad \text{(A2)}$$

$$\text{where, Q}=2.28\left(\frac{\mathrm{E}}{\mathrm{E_m}}\right)^{1.35}$$

For normal incidence, $\theta=0°$ with respect to a surface normal. Eq. (A1) is reduced to the form,

$$Y_{se}=1.114\left[1-\exp\left(-Q\right)\right]\delta_m\left(\frac{E_m}{E}\right)^{0.35} \quad \text{(A3)}$$

A.2. Electron Induced SEY Formulation (Katz) [19]

This formulation is applied in the NASCAP and SPIS software. The estimation of secondary emission yield (Y_{se}) is based on the range and energy loss rate of incident particles:

$$Y_{se}(\theta) = c_1 \int_0^R \left|\frac{dE}{dx}\right| dE \exp(c_2 x \cos\theta) dx \tag{A4}$$

where range R is represented by the sum of two exponentials:

$$R = r_1 E^{n_1} + r_2 E^{n_2} \tag{A5}$$

The range and energy loss rate are related by,

$$\left|\frac{dE}{dx}\right| = \left(\frac{dR}{dE}\right)^{-1} \tag{A6}$$

The above equation can be evaluated with constants c_1 and c_2, determined from the energy maximum yield E_{max} and its corresponding yield $Y_{se\,\text{max}}$ for a given material.

By assuming that dE/dx is constant, Eq. (A4) is evaluated as,

$$Y_{se}(\theta) = c_1 \int_0^{E\frac{dR}{dE}} \left(\frac{dR}{dE}\right)^{-1} \exp(-c_2 x \cos\theta) dx \tag{A7}$$

For isotropic incidence (angle averaged), yield is expressed as,

$$Y_{se}(E) = 2c_1 E \left(\frac{Q - 1 + \exp(-Q)}{Q^2}\right) \tag{A8}$$

where $Q = C_2 E R \frac{dR}{dE}$.

A.3. Ion Induced SEY (Y_{si} Formulation [31]

Y_{si} for isotropic incidence is given as,

$$Y_{si} = (2 - \frac{Q}{2}) 2^{-Q} \delta_1 E^{1/2} \left(1 + \frac{E}{E_m}\right) \tag{A9}$$

$$\text{where, } Q = \begin{cases} 0; & E > 10\,\text{keV} \\ \dfrac{1}{E} - 0.1; & 0.476\,\text{keV} < E < 10\,\text{keV} \\ 2; & E < 0.476\,\text{keV} \end{cases}$$

For normal incidence $\theta = 0°$ with respect to surface normal it is given as,

$$Y_{si} = \delta_1 E^{1/2} \frac{\left(1 + \frac{1}{E_m}\right)}{\left(1 + \frac{E}{E_m}\right)} \tag{A10}$$

Here, δ_1 is the yield at 1 keV, and E_m is the energy for maximum yield.

TABLE A1. BEY for normal incidence.

E (eV)	**BEY (Y_{be})**
$> 100,000$	0.0
10,000–100,000	$1 - 0.7358^{0.037Z}$
1,000–10,000	$1 - 0.7358^{0.037Z} + 0.1 \exp\left(\frac{-E}{5000}\right)$
50–1,000	$0.3338 \ln\left(\frac{E}{50}\right) \left[1 - 0.7358^{0.037Z} + 0.1 \exp\left(\frac{-E}{50}\right)\right]$
< 50	0.0

A.4. Electron Induced BEY formulation [31]

BEY (Y_{be}) can be obtained from incident electron energy and material atomic number (Z) from Table A1.

For isotropic incidence, the normal value of Y_{be} is transformed to,

$$\frac{2(1 - Y_{be} + Y_{be} \times \ln Y_{be})}{\ln^2 Y_{be}} \tag{A11}$$

REFERENCES

[1] Lai, S. T. and R. Pradipta, *Physics of Satellite Surface Charging: Causes, Effects, and Applications*, CRC Press, 2022.

[2] Garrett, H. B. and A. C. Whittlesey, *Guide to Mitigating Spacecraft Charging Effects*, John Wiley & Sons, 2012.

[3] Lu, Y., Q. Shao, H. Yue, and F. Yang, "A review of the space environment effects on spacecraft in different orbits," *IEEE Access*, Vol. 7, 93 473–93 488, 2019.

[4] Hao, J., B. Ru, and J. Fan, "Surface unequal charging effect of GEO satellite," *IEEE Access*, 2023.

[5] Javed, S., N. Rubab, S. Zaheer, S. Poedts, and G. Jaffer, "Numerical calculations of charging threshold at GEO altitudes with two temperature non-extensive electrons," *Space Weather*, Vol. 21, No. 10, e2022SW003412, 2023.

[6] Merenda, K.-D., B. Neufeld, G. Wilson, and T. McDonald, "Spacecraft charging with EMA3D Charge," *Advances in Space Research*, Vol. 72, No. 12, 5626–5635, 2023.

[7] Pervaiz, F., S. Ali, M. Ali, and S. T. Lai, "Spacecraft charging due to energetic electrons and ions at geosynchronous altitudes," *Journal of Geophysical Research: Space Physics*, Vol. 128, No. 1, e2022JA030642, 2023.

[8] Nakamizo, A., M. Nakamura, T. Nagatsuma, Y. Kubota, K. Koga, H. Matsumoto, and Y. Miyoshi, "Development of a surface charging assessment system for the GEO region by combining global magnetosphere MHD and spacecraft charging models," *IEEE Transactions on Plasma Science*, 2025.

[9] Ghosh, S. and A. Chakrabarty, "Estimation of capacitance of different conducting bodies by the method of rectangular subareas," *Journal of Electrostatics*, Vol. 66, No. 3-4, 142–146, 2008.

[10] Alad, R. H. and S. B. Chakrabarty, "Capacitance and surface charge distribution computations for a satellite modeled as a rectangular cuboid and two plates," *Journal of Electrostatics*, Vol. 71, No. 6, 1005–1010, 2013.

[11] Mehta, P. D. and S. B. Chakrabarty, "Electrical capacitance of dielectric coated metallic parallelepiped and closed cylinder isolated in free space," *Journal of Electrostatics*, Vol. 71, No. 4, 756–762, 2013.

[12] Karthikeyan, B., V. K. Hariharan, and S. Sanyal, "Estimation of free space capacitance and body potential of a spacecraft for charging analysis," *IEEE Transactions on Plasma Science*, Vol. 41, No. 12, 3487–3491, 2013.

[13] Alad, R. H. and S. Chakrabarty, "Electrostatic analysis of an artificial orbiting satellite for absolute charging," *IEEE Transactions on Plasma Science*, Vol. 43, No. 9, 2887–2893, 2015.

[14] Pandya, A., P. Mehta, and N. Kothari, "Impact of secondary and backscattered electron currents on absolute charging of structures used in spacecraft," *International Journal of Numerical Modelling: Electronic Networks, Devices and Fields*, Vol. 32, No. 6, e2631, 2019.

[15] Patel, K., R. Alad, A. Pandya, and S. Gupta, "Influence of induced electron yields of ubiquitous materials on absolute charging of GSAT-19," *Nanotechnology Perceptions*, Vol. 20, No. 1, 155–166, 2024.

[16] Alad, R. H. and S. B. Chakrabarty, "Electrostatic modeling of coupled metallic bodies in the shape of a funnel," *Electromagnetics*, Vol. 33, No. 3, 201–220, 2013.

[17] Balanis, C. A., *Antenna Theory and Application*, 4th ed., Willey, 2021.

[18] Whipple, E. C., "Potentials of surfaces in space," *Reports on Progress in Physics*, Vol. 44, No. 11, 1197, 1981.

[19] Katz, I., D. E. Parks, M. J. Mandell, J. M. Harvey, S. S. Wang, M. Rotenberg, *et al.*, "A three dimensional dynamic study of electrostatic charging in materials," Tech. Rep., NASA, 1977.

[20] Muranaka, T., S. Hosoda, J.-H. Kim, S. Hatta, K. Ikeda, T. Hamanaga, M. Cho, H. Usui, H. O. Ueda, K. Koga, and T. Goka, "Development of multi-utility spacecraft charging analysis tool (muscat)," *IEEE Transactions on Plasma Science*, Vol. 36, No. 5, 2336–2349, 2008.

[21] Davis, V. A., M. J. Mandell, D. C. Ferguson, and D. L. Cooke, "Modeling of DMSP surface charging events," *IEEE Transactions on Plasma Science*, Vol. 45, No. 8, 1906–1914, 2017.

[22] Wang, S., X.-J. Tang, Z. Yi, Y.-W. Sun, and Z.-C. Wu, "Transient analysis of spacecraft exposed dielectric charging using SICCE," *IEEE Transactions on Plasma Science*, Vol. 45, No. 2, 275–281, 2017.

[23] Hughes, J. A. and H. Schaub, "Electrostatic tractor analysis using a measured flux model," *Journal of Spacecraft and Rockets*, Vol. 57, No. 2, 207–216, 2020.

[24] Wolfley, O. H., "Simulation of charge collection to spacecraft surfaces: Freja satellite," Tech. Rep., NASA, 2018.

[25] Nakamura, M., S. Nakamura, R. Kawachi, and K. Toyoda, "Assessment of worst GEO plasma environmental models for spacecraft surface charging by SPIS," *Transactions of the Japan Society for Aeronautical and Space Sciences, Aerospace Technology Japan*, Vol. 16, No. 6, 556–560, 2018.

[26] Bengtson, M., J. Hughes, and H. Schaub, "Prospects and challenges for touchless sensing of spacecraft electrostatic potential using electrons," *IEEE Transactions on Plasma Science*, Vol. 47, No. 8, 3673–3681, 2019.

[27] Lundgreen, P. and J. R. Dennison, "Strategies for determining electron yield material parameters for spacecraft charge modeling," *Space Weather*, Vol. 18, No. 4, e2019SW002346, 2020.

[28] Cimino, R., M. Commisso, D. R. Grosso, T. Demma, V. Baglin, R. Flammini, and R. Larciprete, "Nature of the decrease of the secondary-electron yield by electron bombardment and its energy dependence," *Physical Review Letters*, Vol. 109, No. 6, 064801, 2012.

[29] Le Pimpec, F., R. E. Kirby, F. K. King, and M. Pivi, "Electron conditioning of technical aluminium surfaces: Effect on the secondary electron yield," *Journal of Vacuum Science & Technology A*, Vol. 23, No. 6, 1610–1618, 2005.

[30] Wang, S., Z.-C. Wu, X.-J. Tang, Z. Yi, and Y.-W. Sun, "A new charging model for spacecraft exposed dielectric (SICCE)," *IEEE Transactions on Plasma Science*, Vol. 44, No. 3, 289–295, 2016.

[31] Help: EQUIPOT Spacecraft surface charging code, [Online] Available:https://www.spenvis.oma.be/help/background/charging/equipot/equipot.html, Jun. 1 2022.

[32] Gibson, W. C., *The Method of Moments in Electromagnetics*, Chapman and Hall/CRC, 2021.

[33] Carson, E., J. Liesen, and Z. Strakoš, "Towards understanding CG and GMRES through examples," *Linear Algebra and Its Applications*, Vol. 692, 241–291, 2024.

[34] Purvis, C. K., H. B. Garrett, A. C. Whittlesey, and N. J. Stevens, "Design guidelines for assessing and controlling spacecraft charging effects," Tech. Rep., NASA, 1984.

[35] Ferguson, D. C. and I. Katz, "The worst case GEO environment and the frequency of arcs in GEO," *IEEE Transactions on Plasma Science*, Vol. 43, No. 9, 3021–3026, 2015.

[36] Pandya, A., N. Kothari, and R. Alad, "A comparative study of body potential transient profile of geosynchronous orbit spacecraft in single and double maxwellian plasma models," *International Journal of Numerical Modelling: Electronic Networks, Devices and Fields*, Vol. 35, No. 3, e2968, 2022.